Check for updates

NANO · MICRO small
www.small-journal.com

Surfactant-Stripped Semiconducting Polymer Micelles for Tumor Theranostics and Deep Tissue Imaging in the NIR-II Window

Yuanmeng Ding, Byullee Park, Jiamin Ye, Xiaojie Wang, Gengqi Liu, Xingyue Yang, Zhen Jiang, Moongyu Han, Yong Fan, Jibin Song, Chulhong Kim,* and Yumiao Zhang**

Photoacoustic imaging (PA) in the second near infrared (NIR-II) window presents key advantages for deep tissue imaging owing to reduced light scattering and low background signal from biological structures. Here, a thiadiazoloquinoxaline-based semiconducting polymer (SP) with strong absorption in the NIR-II region is reported. After encapsulation of SP in Pluronic F127 (F127) followed by removal of excess surfactant, a dual functional polymer system named surfactant-stripped semiconductor polymeric micelles (SSS-micelles) are generated with water solubility, storage stability, and high photothermal conversion efficiency, permitting tumor theranostics in a mouse model. SSS-micelles have a wideband absorption in the NIR-II window, allowing for the PA imaging at both 1064 and 1300 nm wavelengths. The PA signal of the SSS-micelles can be detected through 6.5 cm of chicken breast tissue in vitro. In mice or rats, SSS-micelles can be visualized in bladder and intestine overlaid 5 cm (signal to noise ratio, SNR ≈ 17 dB) and 5.8 cm (SNR over 10 dB) chicken breast tissue, respectively. This work demonstrates the SSS-micelles as a nanoplatform for deep tissue theranostics.

1. Introduction

Deep tissue imaging is important for preclinical and clinical imaging applications as it provides accurate and timely diagnosis and treatments of various anatomical structure and diseases deep in the body.[1–4] Although positron emission tomography and computed tomography (CT) imaging are not limited by the penetration depth, the non-invasive photoacoustic (PA) imaging modality with high spatial resolution has attracted much recent attention for imaging in deep tissues, something not traditionally possible for an optical imaging modality.[5–8] PA is an emerging hybrid imaging technique that integrates both optical excitation and ultrasonic detection, giving rise to less light scattering and high sensitivity.[9] To further increase the penetration depth, a wide variety of contrast agents have been used for PA imaging including endogenous chromophores, FDA approved methylene blue and indocyanine green, gold nanoparticles, carbon nanotubes, organic nanoparticles, liposomes, and polymeric micelles.[10–12] However, it is still important to develop more enabling agents for theranostics of deep tissues with less scattering such as imaging at longer wavelength.

Recently, imaging in the NIR-II window has gained interest since it has intrinsic advantages including deeper penetration depth, less scattering, and higher maximum permissible exposure.[13–15] Given these merits, fluorescence imaging,[16–19] self-luminescence,[20,21] and PA imaging[22–25] in the NIR-II window have been investigated for various applications including tumor imaging,[16,26–29] blood vessel, and lymph node imaging,[22,26,30–32] specific organ imaging such as bladders and intestines[33,34] and microenvironment imaging of diseases.[35–39] Existing NIR-II PA contrast

Y. Ding, X. Wang, G. Liu, X. Yang, Z. Jiang, Y. Zhang
School of Chemical Engineering and Technology
Key Laboratory of Systems Bioengineering (Ministry of Education)
Tianjin University
Tianjin 300350, China
E-mail: ymzhang88@tju.edu.cn

B. Park, M. Han, C. Kim
Department of Electrical Engineering
Convergence IT Engineering and Mechanical Engineering
Pohang University of Science and Technology
Pohang 37673, Korea
E-mail: chulhong@postech.ac.kr

The ORCID identification number(s) for the author(s) of this article can be found under https://doi.org/10.1002/smll.202104132.

J. Ye, J. Song
College of Chemistry
MOE key Laboratory for Analytical Science of Food Safety and Biology
Institution
Fuzhou University
Fuzhou 350108, China
E-mail: jinbinsong@fzu.edu.cn

Y. Fan
Department of Chemistry
State Key Laboratory of Molecular Engineering of Polymer and IChem
Shanghai Key Laboratory of Molecular Catalysis and Innovative Materials
Fudan University
Fudan 200433, China

DOI: 10.1002/smll.202104132

 © 2021 Wiley-VCH GmbH

agents include metal-base compounds,[40–42] noble metals,[43–45] phosphorous phthalocyanine,[34] semiconducting polymers (SP),[46–49] and others.[50–52] Specifically, imaging of gastrointestinal (GI) tract has attracted interest in recent years, however, due to the acidic, enzymatic, and digestive environments in GI, and the snaking feature of GI tract that is deeply posited in abdomen, imaging of GI tract with high resolution remains a major challenge. To this end, polydopamine-coated down-conversion nanoparticles[53] and lanthanide-based nanoparticles[54] for near-infrared-II fluorescence or PA imaging were reported. Quantum dots,[14] SiO_2 nanoparticles,[54] bioconjugates,[33] protein-based nanoparticles,[55] and AIEgen nanoparticles[56] have been explored for the use as imaging agents for intestinal imaging or imaging in the NIR-II region in deep penetration depth. Multimodal imaging methods such as CT/MRI using PEGylated BaGdF5 was also reported for efficient GI imaging.[57] NIR-II chromophores also show promise for bladder imaging with high penetration depth, as well as photothermal therapies and combinational immunotherapy for cancer theranostics.[58–61]

In order to achieve high penetration depth, new imaging system that is able to detect up to 8 cm of phantom or through live rats were developed.[62] Also, surfactant-stripped cyanine micelles were developed for PA imaging through 12 cm of chicken breast tissue in a phantom study.[8] Also, biocompatible nickel dithiolene-based polymeric nanoparticles were designed and up to 3.4 cm of in vivo imaging depth was achieved.[4] SP are another important type of PA contrast agent for the imaging at the NIR-II window given the flexible chemical structures with good tunability and the great promise for molecular imaging of cells,[63] tumors,[64–66] reactive oxygen species,[67] and others. There have been reports on deep tissue PA imaging using SPs with 5 cm imaging depth in a chicken breast phantom study using low concentration of thienoisoindigo-based SP.[6]

In this study, we designed and synthesized a new SP with TTQ as the electron withdrawing acceptor and alkyl-fluorene as the electron donor. Using temperature-sensitive block copolymer, Pluronic F127 as the carrier of the SP, and the corresponding water-soluble formulation of surfactant-stripped SP (SSS-micelles) was generated. Unlike the small molecules we previously used formulated by a low-temperature critical micelle concentration (CMC)-switching approach for multimodal gut imaging[68,69] and microbiota fluorescence imaging,[56] the newly designed SP chromophore encapsulated in SSS-micelles in this study, exhibited a prominent NIR-II absorption range from 1000 to 1400 nm and high photothermal conversion, enabling the applications of tumor theranostics and deep tissue imaging by PA. SSS-micelles provide strong contrast for PA imaging of murine tumors at 1300 nm and tumors were effectively eradicated by photothermal therapy (PTT) at 1064 nm excitation. Deep tissue imaging was realized using SSS-micelles. In a phantom imaging experiment, PA signal of SSS-micelles embedded in 6.5 cm chicken breast tissue could be detectable (signal to noise ratio, SNR ≈ 20 dB) using 1064 nm laser. An imaging depth of 5 cm was also achieved for PA imaging of the bladder of rats with chicken breast tissue overlaid. In addition, intestinal mapping of mice was clearly outlined by PA imaging following gavage of concentrated SSS-micelles with 5.8 cm (SNR over 10 dB) of chicken breast overlaid on the abdomen. SP-based SSS-micelles warrant the investigations of the tumor theranostics and deep tissue imaging at longer wavelength in the NIR-II window.

2. Results and Discussion

2.1. Generation of Concentrated SSS-Micelles

We designed and synthesized a novel thiadiazoloquinoxaline (TQ)-based SP by a three-step chemical reaction using Pd-catalyzed Stille Coupling. The synthetic route of SP and the ^{1}H-NMR, ^{13}C-NMR, mass spectra analysis were shown in Figures S1–S8, Supporting Information. The chemical structure of SP consists of alternating donor and acceptor units as shown in **Figure 1**A. In addition, the high molecular weight (3593 g moL^{-1}) and low polydispersity coefficient (PDI = 1.49) of SP was confirmed by gel permeation chromatography (GPC) (Figure S9, Supporting Information). Next, to improve the water solubility and biocompatibility of SP, FDA-approved block copolymer Pluronic F127 (F127) was used to encapsulate SP to form semiconducting polymeric nanoparticles via nanoprecipitation method. Because the F127 micellization process is temperature-sensitive, free micelles would dissociate into unimers at low temperature. Therefore, free F127 could be stripped away at low temperature, generating the purified and concentrated surfactant-stripped semiconducting micelles (SSS-micelles, Figure 1B). As shown in Figure 1C, the absorption spectrum of the obtained SSS-micelles solution has broad absorption band at 800–1600 nm with the strongest absorption at 1255 nm. Compared to SP in tetrahydrofuran (THF) having highest absorption at 1243 nm, the spectral absorption curve exhibited slightly red shift. The reason for choosing F127 to solubilize SP is that the CMC of F127 is temperature-sensitive. The ultrafiltration at low-temperature can effectively concentrate the SSS-micelles solution, giving rise to ultrahigh absorption of SSS-micelles. Moreover the molar extinction coefficient of the SSS-micelles was calculated as 16.8 ± 0.5 mL $(mg.cm)^{-1}$,almost the same level as the previously reported.[6] As showed in Figure 1D, using this approach, the calculated absorption of SSS-micelles at 1064 nm can reach up to 1197, ≈1000 times higher than the absorption before low-temperature processing, which is significantly useful for deep tissue imaging. To verify the advantage of F127-solubilized SSS-micelles, the other two commercially available surfactants, Tween 80, and Cremophor EL, were selected to solubilize SP, then subject to the same low-temperature washing process. The absorption F127-solubilized SSS-micelles at 1064 nm was significantly higher than Tween-80 or Cremophor-solubilized SP (Figure 1E).

2.2. The Physical and Optical Properties of SSS-Micelles

To further investigate the physical and optical properties of SSS-micelles, the size and morphology of SSS-micelles were characterized by dynamic light scattering (DLS) and transmission electron microscopy (TEM). The hydrodynamic diameter of SSS-micelles was ≈67 nm with a low polydispersity index (PDI) of 0.12 (**Figure 2**A). A spherical morphology of

© 2021 Wiley-VCH GmbH

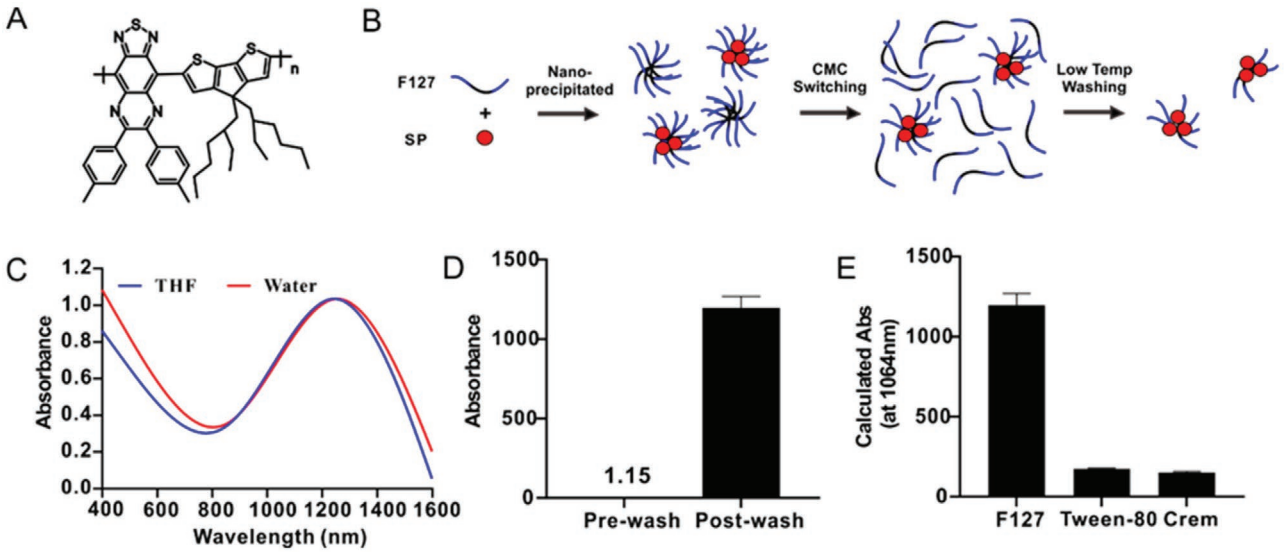

Figure 1. Generation of concentrated SSS-micelles with strong absorbance in the NIR-II window. A) The chemical structure of the synthesized SP. B) Illustration of the formation process of SSS-micelles by low-temperature surfactant striping method. C) The absorption spectrum of SP in THF and SSS-micelles aqueous solution. D) The absorption of SSS-micelles before and after washing ($n = 3$). E) The calculated absorption of SP of the same mass encapsulated by different surfactants including F127, Tween 80, and Cremophore EL after concentration at 1064 nm ($n = 3$).

SSS-micelles was observed by TEM, with a size consistent with DLS (Figure 2B). The size and PDI remained almost the same over 14 days measured by DLS, as shown in Figure 2C,D. Furthermore, SPNs can still maintain good stability in simulated gastric fluid and simulated intestinal fluid (Figure S10, Supporting Information), this result is consistent with our previous finding.[69,70]

The PA and photothermal properties of SSS-micelles were studied. SSS-micelles exhibited significant PA signals in the NIR-II window as shown in Figure 2E, and the curve of PA signal at different wavelengths has a similar pattern as the absorption spectrum. Subsequently, NIR-II photothermal effect of SSS-micelles was evaluated. Different concentrations of SSS-micelles in aqueous solutions were irradiated by a 1064 nm laser for 5 min and the temperature was monitored using an infrared camera (Figure S11, Supporting Information). As demonstrated in Figure 2F, the temperature of the SSS-micelles with different concentrations increases as the irradiation time increases. When 0.5 mg mL^{-1} of SSS-micelles was irradiated by a 1064 nm laser for 5 min, the solution temperature can reach as high as 86 °C. By contrast, the temperature of PBS solution is almost unchanged under the same irradiate conditions. The photothermal stability of SSS-micelles was examined as well and five heat-cool temperature cycles of SSS-micelles solution were acquired by controlling laser on or off. The same temperature change trend was observed during the five heat-cool curves, indicating the good photothermal reversibility of SSS-micelles (Figure 2G). Also, the photothermal conversion efficiency of SSS-micelles was calculated to be 27% in accordance with the cooling process (Figure S12, Supporting Information). These results verified the prominent photothermal properties and excellent photothermal stability of SSS-micelles, showing their promise for NIR-II PA imaging and PTT.

Prior to in vivo study, in vitro PTT effect in the NIR-II window and cell cytotoxicity were investigated. 4T1 tumor cells were selected and incubated for 24 h with media containing different concentrations of SSS-micelles with or without 1064 nm laser irradiation (5 min, 1 W cm^{-2}) and the standard CCK8 was utilized to evaluate cell toxicity. As shown in Figure 2H, no significant cytotoxicity was observed when the concentration of SSS-micelles is up to at least 0.1 mg mL^{-1} without laser irradiation. But with laser treatment, significant apoptosis was observed when concentration is over 0.05 mg mL^{-1}. Next, live/dead cell staining experiment was carried out to study the PTT effect of SSS-micelles, calceinacetoxymethyl (green) dyes, and propidium iodide (red) dyes were used to stain live and dead cells, respectively. In Figure 2I, strong green fluorescence was observed in cells treated with PBS, PBS+laser, and SSS-micelles only group, indicating that the 1064 nm laser irradiation or the SSS-micelles alone at the experimental condition did not affect cell survival. But all of the cells treated with both SSS-micelles and laser displayed red fluorescence, demonstrating the phototoxicity caused by SSS-micelles. These results highlight the cytotoxic photothermal properties of SSS-micelles and the potential of SSS-micelles for PTT for tumor treatment.

2.3. Tumor Imaging and Photothermal Therapy

We next investigated the PA imaging of tumors in vivo in the NIR-II window and photothermal treatment capabilities using SSS-micelles. PA imaging of tumor was performed at 1300 nm, which was close to the maximum absorption of SSS-micelles (Figure 1C). SSS-micelles (2 mg mL^{-1}, 200 µL) were injected intravenously into tumor-bearing mice, and the tumor regions of the mouse were immediately imaged, and subsequently PA imaging of the same region was captured at 4, 8, 12, 24, 48 h after injection, meanwhile PA signal values were recorded. As shown in **Figure 3**A,B, the PA signal in the mouse tumor area gradually increased and the PA signal reached the maximum at

© 2021 Wiley-VCH GmbH

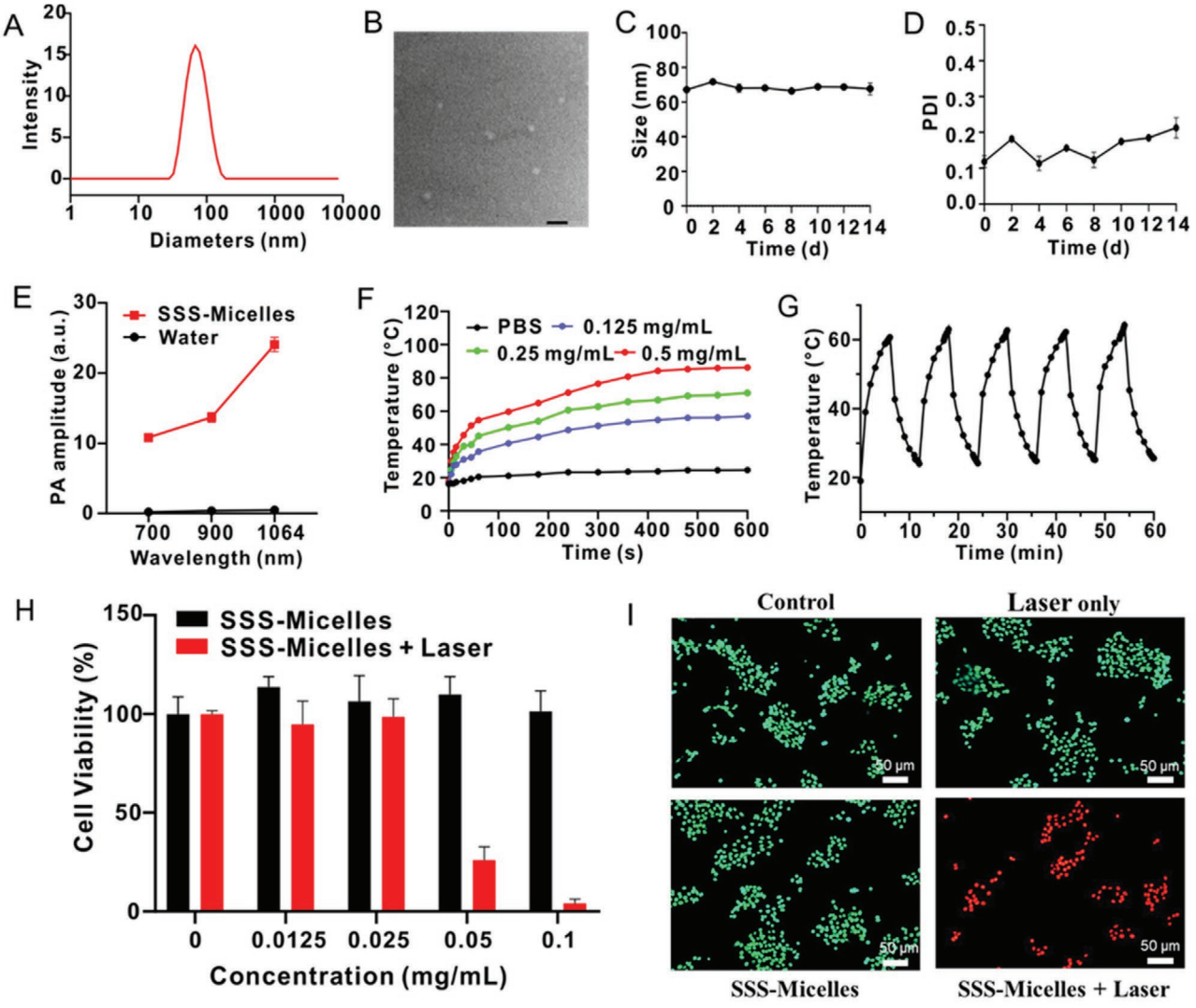

Figure 2. Physical and optical properties of SSS-micelles. A) Hydrodynamic diameters of SSS-micelles measured by DLS. B) TEM image of SSS-micelles, scale bar: 200 nm. C) Size stability of SSS-micelles within 14 days monitored by DLS ($n = 3$). D) PDI changes of SSS-micelles aqueous solution during two weeks of storage ($n = 3$). E) PA spectrum of SSS-micelles in water ($n = 3$). F) The temperature change curve of SSS-micelles solution with different concentrations under a 1064 nm laser irradiation at 1 W cm^{-2}. G) Heating and cooling curve acquired by the laser on or off alternately. H) Viability of cells incubated at different SSS-micelles concentrations with or without laser treatment ($n = 3$). I) Representative fluorescence micrographs of 4T1 tumor cells live/dead stained after treatment with PBS, PBS+laser, SSS-micelles, or SSS-micelles+laser as indicated.

24 h post-injection. The PA signal increased by five times compared to the control group, this indicated the accumulation of SSS-micelles in the tumor reached the maximum at 24 h after injection, which is probably attributed to enhanced permeability and retention effect.[71] In addition, endocytosis of nanoparticles into 4T1 cells was previously reported.[72] Thus, SSS-micelles can be used for PA imaging of tumors and 24 h after injection was the ideal time point for tumor photo-treatments. In addition to the in vivo imaging by PA modality, tumors were also excised and ex vivo imaged modality by fluorescence approach. In order to fluorescently label SSS-micelles, we chemically convert hydroxyl groups of Pluronic F127 to amines, so that fluorescein isothiocyanate (FITC) could be easily conjugated to the surface of SSS-micelles in aqueous solution (Figure S13, Supporting Information). As shown in Figure S14, Supporting Information, significant fluorescence was observed in tumors that were excised 24 hours after mice were intravenously injected FITC-labeled SSS-micelles.

SSS-micelles could not only be used as contrast agent for tumor imaging, but also could be used for tumor PTT. The photothermal effect was demonstrated in vitro in Figure 2F–I, we next studied the potential use of SSS-micelles for tumor therapy in vivo. 4T1 xenograft tumor mice were prepared and randomly divided into four groups including PBS, SSS-micelles, PBS+laser, and SSS-micelles+laser ($n = 5$ per group). Upon laser irradiation, SSS-micelles effectively converted light into heat, leading to the temperature increase in the tumor region and eventually the death of tumor cells. The temperature of the tumor surface was recorded using an infrared camera during treatment 24 h after mice were treated with laser

© 2021 Wiley-VCH GmbH

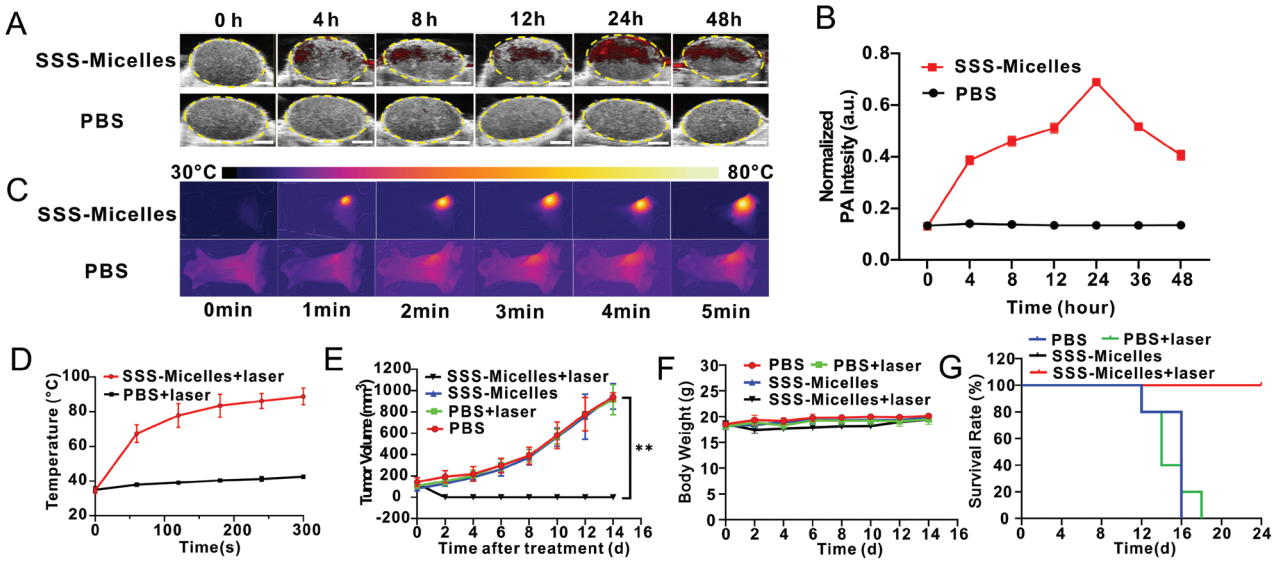

Figure 3. Tumor theranostics using SSS-micelles. A) Tumor PA images of tumor-bearing mouse at different time points after treatment by PBS (200 µL) or SSS-micelles (2 mg mL^{-1}, 200 µL, Scale bar: 2 mm). B) Changes of PA intensity of the tumor over time. C) Infrared thermal images of tumor-bearing mice given PBS (200 µL) or SSS-micelles (2 mg mL^{-1}, 200 µL) with irradiation with a 1064 nm laser (1 W cm^{-2}). D) Tumor temperature changes under 1064 nm laser irradiation (1 W cm^{-2}, $n = 5$). E) Tumor volume and F) Body weight of mice treated with PBS (200 µL), SSS-micelles (200 µL, 2 mg mL^{-1}), PBS+laser (200 µL, 1 W cm^{-2}), and SSS-micelles+laser (200 µL, 2 mg mL^{-1}, 1 W cm^{-2}) as indicated ($n = 5$). G) Survival rate of tumor-bearing mice treated with PBS, SSS-micelles, PBS+laser, and SSS-micelles+laser as indicated. *t*-test analysis of variance was used to analyze significant difference, ** $p < 0.01$.

and SSS-micelles (or PBS as control) as displayed in Figure 3C. In the PBS+laser group, the temperature of the tumor area has only slightly increased whereas the temperature of the tumor in the SSS-micelles+laser group increased significantly and the maximum temperature could reach 88 °C after laser irradiation for 5 min (Figure 3D). Laser was controlled to only shed to the tumor region to avoid burning the health tissues. In order to further evaluate the efficacy of tumor treatment, we examined the tumor size and body weight of mice in all groups every other day. The tumors in the SSS-micelles group were fully ablated without regrowth, leaving only black scabs (Figure S15, Supporting Information), whereas the tumor volume of mice in the other three groups continued to increase more than ten times within 14 days (Figure 3E). Mice in the SSS-micelles+laser group lost a small amount of weight immediately after treatment, but quickly rebounded to the same levels as other group (Figure 3F). The Kaplan–Meier survival curves was displayed in Figure 3G. Compared with other control groups where mice all died within 16 days, all mice in the SSS-micelles+laser group remained alive without noticing any abnormal behaviors or tumor recurrence before being sacrificed on day 24. In addition, biodistribution in different organs of tumor-bearing mice after intravenous administration of FITC-labeled SSS-micelles was demonstrated in Figure S16, Supporting Information. Significant accumulation of SSS-micelles in tumor and slight accumulation in liver were observed at 24 h after administration of SSS-micelles, but no fluorescence was seen in all organs after 4 days, likely because all SSS-micelles could be cleared out by at most 4 days (Figure S16, Supporting Information). It was previously reported that the SP-based nanoparticles could be metabolically degraded by enzymes such as peroxidase and lipase into small segments, followed by elimination by hepatobiliary or renal pathways eventually.[66]

2.4. Toxicity

Given the promising therapeutic efficacy, the toxicity of SSS-micelles was then assessed in outbred CD-1 mice (6–8 weeks old). The mice were divided into two groups, SSS-micelles (2 mg mL^{-1}, 200 µL) or PBS were intravenously administered to mice via tail vein injection. After 14 days, blood and organs were collected for complete blood count (CBC) analysis, serum chemistry profile and histological hematoxylin and eosin (H&E) analysis. As shown in **Figure 4**A,B. There were no significant differences for the CBC parameters between SSS-micelles-injected mice and the control mice including white blood cells (WBC), lymphocytes (LYM), red blood cell (RBC) count, mean cell volume (MCV), etc. Serum markers such as blood urea nitrogen and alanine aminotransferase, were also in the normal ranges as in the control group, indicative of no nephrotoxicity or hepatoxicity. Major organs of the mice treated with SSS-micelles were examined by H&E staining analysis and no inflammation or other abnormality was observed (Figure 4C). This suggests that SSS-micelles (2 mg mL^{-1}, 200 µL) did not cause any acute toxicity.

2.5. Deep Tissue PA Imaging in Mice or Rats

We next investigated the use of SSS-micelles for deep tissue PA imaging, using a 1064 nm laser system with stronger laser pulse energy. We first did an in vitro penetration depth experiment using the phantom of chicken breast as shown in Figure S17, Supporting Information. The PA signal of concentrated SSS-micelles (60 mg mL^{-1}) was detected through 6.5 cm chicken breast tissue, which is frequently used for mimicking human breast tissue in many studies. According to the previous literature, the 1/e optical penetration depths in human

© 2021 Wiley-VCH GmbH

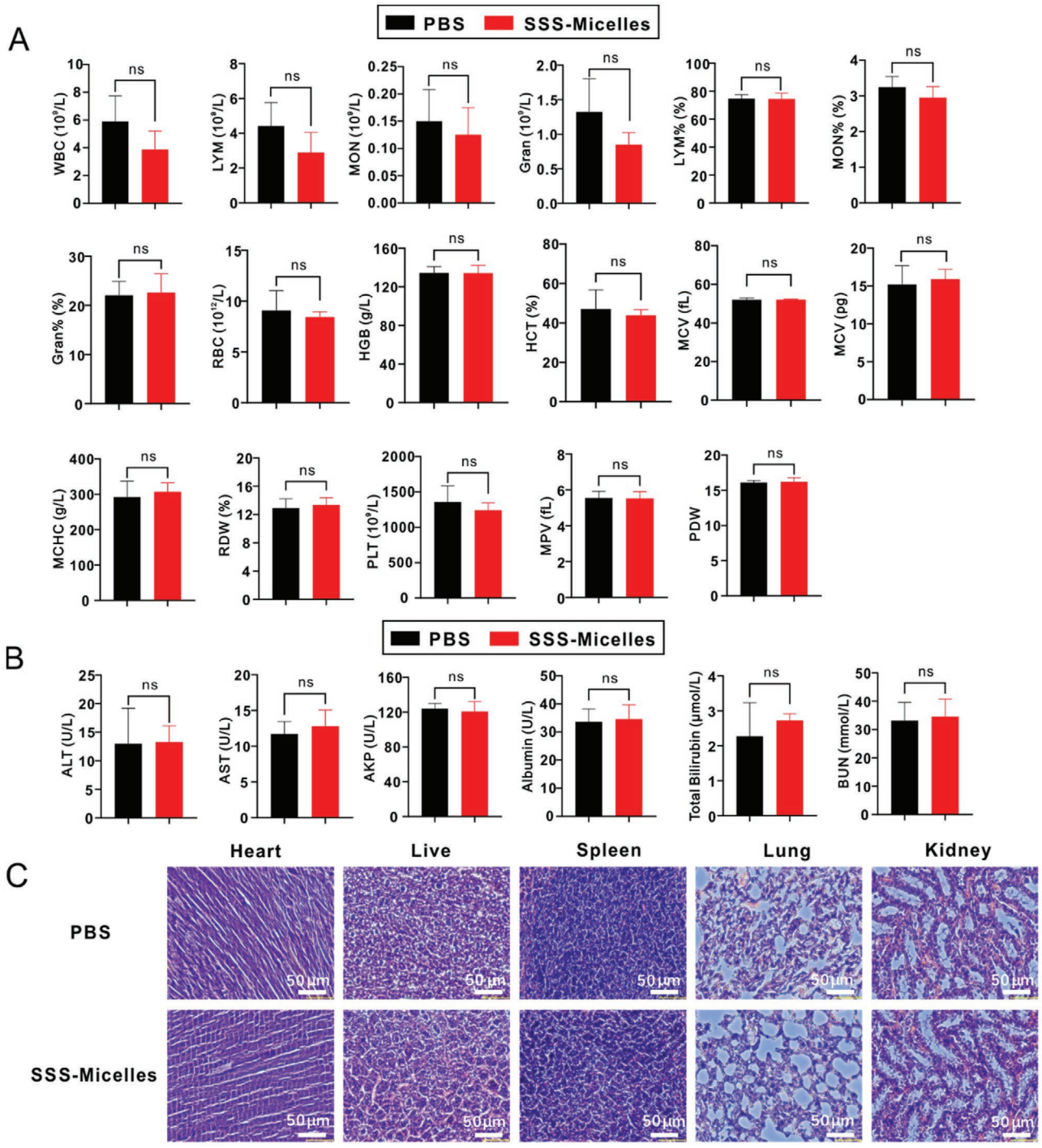

Figure 4. Toxicity analysis of SSS-micelles. A) Complete blood cell count analysis and B) serum chemistry profile of CD-1 mice injected with 200 μL SSS-micelles (2 mg mL^{-1}) or PBS. One injection was given on day 0,blood and organs were collected on day 14. Data was analyzed via *t*-test analysis of variance, ns $p > 0.05$. C) H&E staining analysis of major organs ($n = 4$). Standard range of mouse CBC: WBC: 0.8–6.8, LYM: 0.7–5.7, MON: 0–0.3,Gran: 0.1–1.8, LYM%: 55.8–90.6, MON%: 1.8–6.0, Gran%: 8.6–38.9, RBC: 6.36–9.42, HGB: 110–143, HCT: 34.6–44.6, MCV: 48.2–58.3, MCH: 302–353, RDW: 13–17, PLT: 450–1590, MPV: 3.8–6).

breast tissue and chicken breast tissue are 0.53 cm at 980 nm and 0.58–0.95 cm at 1064 nm, respectively.[4,73] This is comparable to the calculated 1/e penetration depth of 0.54 cm at 1064 nm based on our experimental results. The noise equivalent depth is 10.8 cm, which is 20 times deeper than our 1/e penetration depth. Then we moved onto the in vivo imaging of the bladder in a rat model and intestine in a mouse model. The concentrated SSS-micelles were administered to the bladder of rats or intestine of mice via transurethral injection or gavage, respectively. A certain thickness of chicken breast

© 2021 Wiley-VCH GmbH

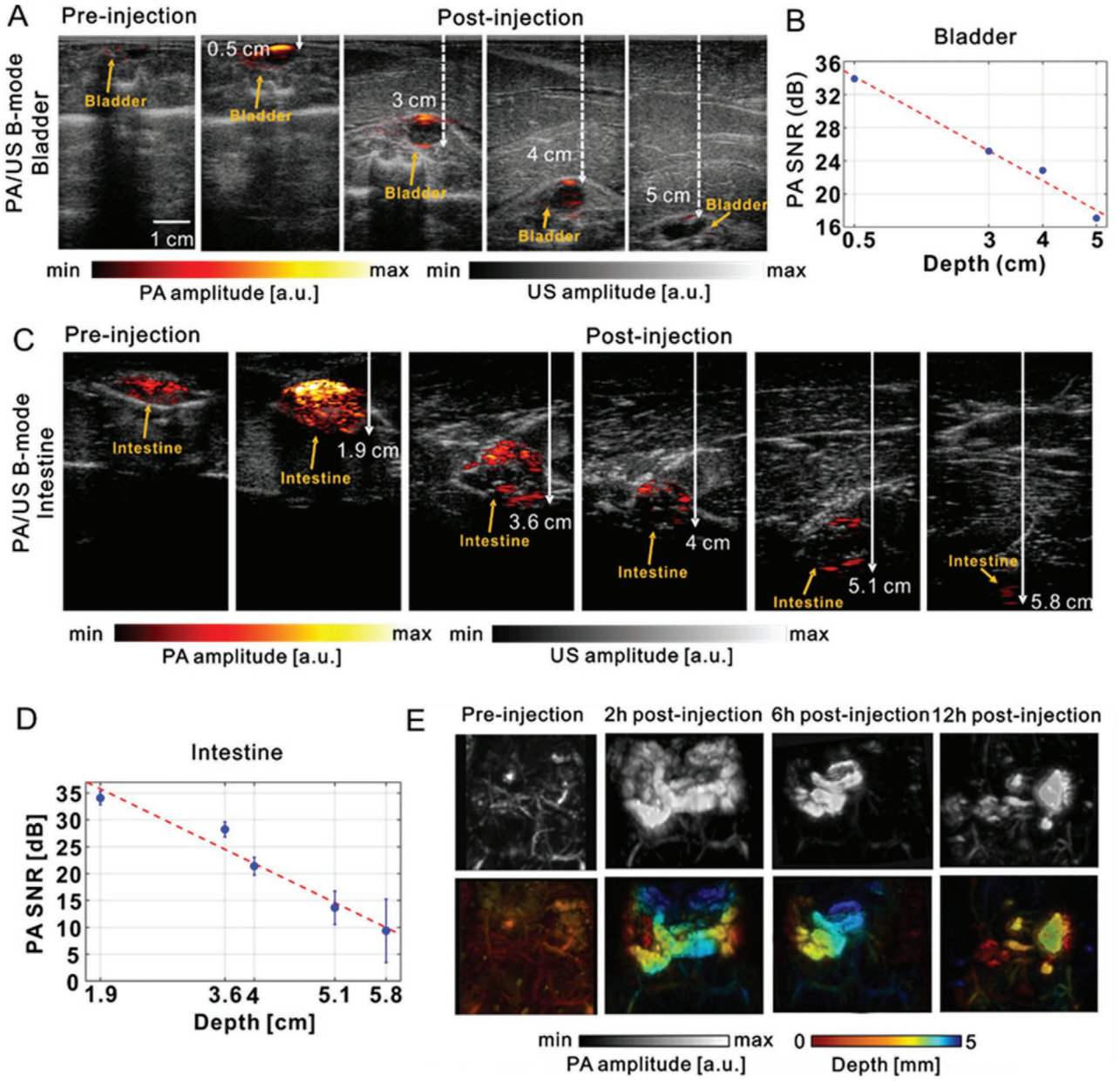

Figure 5. Deep tissue PA imaging with 1064 nm laser excitation. A) PA imaging of bladder in rats with different thicknesses (0.5 cm, 3 cm, 4 cm, 5 cm) of chicken breast tissues stacked on rats after urethral injection of concentrated SSS-micelles (56 mg mL^{-1}, 200 µL). B) The signal-to-noise ratio with different depths in A. C) PA imaging of intestine in rats with different thicknesses (0.5 cm, 3 cm, 4 cm, 5 cm) of chicken breast tissues stacked on rats after rats were gavaged SSS-micelles (56 mg mL^{-1}, 20 µL). D) The signal-to-noise ratio with different depths in C ($n = 3$). E) PA images (above) and corresponding depth-encoded image (below) of rat intestine after gavage of concentrated SSS-micelles (56 mg mL^{-1}, 20 µL) at various timepoints (0 h, 2 h, 6 h, 12 h). Details of the above experiment: pulsed laser: 1064 nm, transducer: 128 linear, 8.5 MHz (Fc), laser fluence: ≈70–80 mJ cm^{-2}.

tissue was stacked on the abdomen as shown in Figure S18, Supporting Information, (for bladder imaging) and Figure S19, Supporting Information, (for intestinal imaging). The bladder or intestinal imaging and the corresponding SNR under different chicken tissue thickness were demonstrated in **Figure 5**A,B (for bladder) and Figure 5C,D (for intestine). The PA signal of SSS-micelles in the bladder was still be detectable when the imaging depth was up to 5 cm (SNR ≈ 17 dB). Similarly, SSS-micelles in the intestine under up to 5.8 cm (SNR over 10 dB) chicken breast tissue was still be detectable. In addition, SSS-micelles also showed advantages in intestinal mapping with high resolution. As demonstrated in Figure 5E, the transit of SSS-micelles in the intestine over time (pre-injection and 2, 6, and 12 h of post-injection) was clearly visible in the intestine contour images with pseudo color-coded depth.[74] The safety of orally administered SSS-micelles for intestinal imaging was then assessed using CD-1 mice (6–8 weeks of age). The analysis of serum chemistry

© 2021 Wiley-VCH GmbH

showed no significant toxicity even the mice were orally given twofold of imaging dose as shown in Figure S20, Supporting Information, which is not surprising because most of contrast agents might be excreted out in feces, as previously demonstrated.[69] For the imaging of bladder, similarly, it was previously showed that contrast agent after transurethral injection could be rapidly excreted out in urine within 1–3 hours.[75] Taken these together, it can be concluded that SSS-micelles showed its great promise for the deep tissue imaging thanks to the high concentration of SSS-micelles prepared by the low-temperature surfactant stripping approach, providing strong absorption signals in the second NIR window.

3. Conclusion

In this work, a novel TQ-based SP with a longer absorption wavelength was successfully synthesized via Pd-catalyzed Stille coupling. The deliberately designed SP effectively transfers the absorption band to the NIR-II region with the maximum absorption at ≈1300 nm. The combination of CMC-switching approach and this new SP with a longer absorption wavelength is significantly useful for NIR-II imaging. This donor–acceptor structure is chemically flexible with high tunablity, subjected to numerous combinations of rational designs. Also, other imaging moieties such as fluorescence imaging moieties, and the combinations of NIR-I and NIR-II properties could be incorporated into this type of backbones. Furthermore, the terminal hydroxyl groups of Pluronic could be chemically modified with ease. Amine-containing F127 was made in this work, showing the great potential of actively targeting tumor by conjugation of targeting ligands such as folate and antibody. In summary, SSS-micelles present a new class of formulation strategy and enabled the NIR-II active polymer to be concentrated to ultrahigh absorptions and concentration values, enabled by the unique processing made possible by the temperature-sensitivity of the F127. SSS-micelles exhibited physiological stability and strong photothermal properties. Using SSS-micelles, PA imaging of tumors was possible, as well as potent tumor eradication via photothermal treatment with a 1064 nm light source. Notably, SSS-micelles were demonstrated for deep tissue imaging with the penetration depths of 6.5 and 5.8 cm for the in vitro and in vivo imaging, respectively. SSS-micelles showcase the utility of novel polymer approaches in both forming the active SP NIR-II chromophore and also formulating it with F127 to high concentrations. Future directions of research may include further investigation on the relationship of polymer structure and efficiency of polymer contrast agents for improved selectivity and resolution of imaging.

4. Experimental Section

Synthesis of Compound 2: Compound 1 (1 g, 2.6 mmol) was dissolved in acetic acid, then iron powder (1.75 g, 31.25 mmol) was introduced to the solution under stirring. The reaction mixture was stirred at room temperature for 24 h. After the reaction was completed, the product was precipitated in ice water and then washed by distilled water and methanol several times in sequence. The final yellow solid, (compound 2) was obtained with 70% yield.

Synthesis of Compound 4: Compound 2 (1 g, 3.08 mmol) was added to an oven-dried three-necked round flask equipped with water condenser. This system was repeatedly filled with helium several times. Then the acetic acid (100 mL) degassed with helium beforehand and compound 3 (0.88 g, 3.68 mmol) was subsequently introduced. The system was pumped with helium and the mixture was subject to magnetic stirring at 100 °C for 12 h. After cooling to room temperature, the mixture was added into water and extracted by dichloromethane (3 × 100 mL). The organic solution was collected and washed with saturated brine, then dried with sodium sulfate for 4 h. The solvent was removed by rotary evaporation. The obtained crude product was dissolved in dichloromethane and purified by silica gel column (eluent solution of DCM: Hexane in a 6:4 ratio). Compound 4 was obtained as orange solid with a yield of 62%.

Synthesis of Compound 6: The same reaction device as the second reaction was prepared. This system was repeatedly pumped with helium several times. The mixture include compound 4 (105.25 g, 0.2 mmol), compound 5 (145.66 g, 0.2 mmol), $Pd_2(dba)_3$ (3.66 mg, 4 µmol), and $P(o\text{-}tol)_3$ (9.74 mg, 32 µmol), which were dissolved in N,N-Dimethylformamide (20 mL) and added into a three-necked round-bottom flask. The reaction mixture solution was vigorously stirred at 100 °C for 48 h under helium atmosphere. Then the resulting mixture was cooled to room temperature, and added dropwise to excess methanol to precipitate crude product. The final product SP was obtained after washing by methanol three times and vacuum drying.[30] Yield: 56%.

Synthesis of SSS-Micelles: 0.5 mg of SP was dissolved in 1 mL THF, then the solution was added into 1.5 mg mL^{-1} Pluronic F127 aqueous solution (10 mL) under sonication for 3 min. Next, the solvent of THF was removed and 100 mL distilled water was added. Then the aqueous solution was filtered with a 0.45 µm polyethersulfone filter membrane to remove large particles of impurities. Finally, the resulting aqueous solution was subjected to ultracentrifugation three times with centrifugation tubes with membrane molecular weight cut off of 100 000 Dalton at 2800 rpm for 10 min.[24,77] The obtained SSS-micelles aqueous solutions were stored at 4 °C for further use.

Synthesis of F127-NH_2: F127 (12.6 g, 1 mmol) was dissolved in anhydrous acetonitrile (15 mL), N,N′-Carbonyldiimidazole (CDI) (1.62 g, 10 mmol) in acetonitrile solution was added dropwise to the solution above, and then stirred at room temperature under nitrogen atmosphere for 4 h. Then the mixed solution was concentrated by evaporation and introduced into excess ethyl ether, this process was repeated three times to remove unreacted CDI. F127-CDI was collected by vacuum drying. The dried F127-CDI (12.7 g, 1 mmol) was dissolved in anhydrous acetonitrile (15 mL), 1,2-ethylenediamine (10 mL) was added dropwise to it, and the mixture was left for reaction overnight at room temperature. After the reaction was complete, the unreacted 1,2-ethylenediamine was removed by rotary evaporation, the acquired crude product was precipitated in excess ethyl ether, this process was repeated three times, and finally F127-NH_2 was obtained through vacuum drying.

Synthesis of FITC-Labeled SSS-Micelles: The SSS-micelles was synthesized using the above-mentioned method, except that the F127 aqueous solution is replaced with F127-NH_2. Then the pH of SSS-micelles aqueous solution was adjusted to 10. 10 µL DMSO solution containing 0.58 mg FITC was added dropwise and the mixture solution was allowed to react overnight at room temperature. The resulting solution was subjected to ultracentrifugation three times with centrifugation tubes with membrane molecular weight cut off of 100 000 Dalton at 2800 rpm for 10 min to remove unreacted FITC, the obtained SSS-micelles aqueous solutions were stored at 4 °C for further use.

Characterization of SSS-Micelles: All intermediate products and SP were confirmed by nuclear magnetic resonance (NMR) spectroscopy (AVANCE IIITM HD 400 MHz NanoBAY). GPC, Malvern VISCOTEK TDA, were used to characterize the molecular weight and polydispersity coefficient of SP using THF as the eluent. The absorption spectra were obtained using spectrophotometer. DLS, a Nano ZS90 Zetasizer (Malvern Instruments), was used to measure the size and size distribution of nanoparticles. TEM images were acquired using TEM (JEM-2100 F, Japan) with negatively staining by 1% sodium phosphotungstate.

© 2021 Wiley-VCH GmbH

Photothermal Property of SSS-Micelles: A series of SSS-micelles aqueous solutions with different concentration gradients (0, 0.125, 0.25, 0.5 mg mL^{-1}) were prepared in 0.5 mL centrifuge tubes. A FLIR ONE infrared camera was used to record the temperature change of the solutions at different timepoints under1064 nm laser irradiation (1 W cm^{-2}). FLIR Tools software was used for thermal imaging analysis.

The photothermal reversibility of SSS-micelles was carried out by recording its temperature change when the SSS-micelles aqueous solution in tube was irradiated by 1064 nm laser during five cycles of laser on/off. Specifically, the SSS-micelles aqueous solution was irradiated under 1064 nm laser at a power density of 1 W cm^{-2}, for 6 min, then the solution was cooled down with laser off for 6 min. Laser on and off were repeated five times alternately, meanwhile the temperature change of the solution was recorded by the infrared camera.

Cell Experiments: Murine breast cancer cell line (4T1) cells were used and cultured in 1640 medium supplemented with 10% FBS under 37 °C and 5% CO_2 atmosphere.

In Vitro PTT: To investigate SSS-micelles' photothermal ability to ablate tumor cells, the 4T1 cells were seeded onto 96-well plates with a density of 1×10^4 cell/wells and incubated for 24 h. Then the medium was removed, the fresh 1640 medium containing various concentrations (0, 0.0125, 0.025, 0.05, 0.1 mg mL^{-1}) was introduced, and cultured for ≈4 h. After irradiation by 1064 nm laser (1 W cm^{-2}) for 5 min, the cells were subject to culture for 20 h. After the incubation, a standard CCK8 assay was carried out to evaluate cell viability.

Live/Dead Cell Staining: 4T1 cells were seeded in 24-well plates and incubated for 24 h, then the medium was changed to the fresh 1640 medium containing 0.1 mg mL^{-1} SSS-micelles, followed by incubation for 4 h. After irradiation by 1064 nm laser, the cells were incubated for another 20 h. After that, the 4T1 cells were stained with Calcein AM and Propidium iodide according to live/dead viability/cytotoxicity assay kit. Live and dead cells were then visually imaged under the fluorescence microscope.

Animal Model: Female BALB/c mice (18 ± 2 g, 7–8 weeks) were purchased from Charles River Beijing Co., Ltd (Beijing, China). The mice received care complying with the policy of the National Institutes of Health guide for the care and use of Laboratory animals and animal protocols were approved by Tianjin University Institutional Animal Care and Use Committee (Protocol number: TJUE-2021-145). Tumors were established by injecting 4T1 tumor cells subcutaneously into the back of mice. Established tumor models were used for subsequent the PA imaging and the PTT of tumor in the NIR-II window.

In Vivo Tumor PA Imaging: The PA imaging of tumor in the NIR-II region was performed when mouse tumor volume reached 100–120 mm^3. After mice were intravenously injected with 2 mg mL^{-1} 200 µL SSS-micelles aqueous solution, the tumor region of the mouse was imaged at predetermined time points (0 h, 4 h, 8 h, 12 h, 24 h, 36 h) by Vevo LAZR-X 3100 PA imaging system (Fujifilm Visual Sonical Co. Ltd, Toronto, Canada) which the PA excitation wavelength was set as 1300 nm.

In Vivo Photothermal Therapy: The 4T1 tumor-bearing mouse were randomly divided into 4 groups treated by PBS only, PBS+laser, SSS-micelles only, and SSS-micelles+laser. $n = 5$ for each group. 2 mg mL^{-1} 200 µL SSS-micelles aqueous solution was intravenously injected into mice in SSS-micelles group via tail vein, while the mice in PBS group were intravenously injected with the same amount of PBS, when the tumor volume of the established mouse model reached 100–120 mm^3. At 24 h after injection, the tumor sites of the mice were exposure to a 1064 nm laser at 1 W cm^{-2} for 5 min. Infrared camera (FLIR ONE T810402) was used to monitor the temperature variation of the tumor region. Tumor volume and body weight in each group were recorded every two days. The tumor volume was calculated according to the equation: tumor volume = 0.5 × length × $width^2$. All mice were sacrificed on day 14 after PTT, and the tumors tissues were collected for further use.

Biodistribution: 200 µL, 1 mg mL^{-1} FITC-labeled SSS-micelles aqueous solution was intravenously injected into tumor-bearing nude mice (n = 3/group) via tail vein. Mice were euthanized and organs (including heart, liver, spleen, lung, kidney) and tumor were collected at one and four days after injection. Fluorescence imaging of organs and tumor was performed with an automated in vivo imaging system (Maestro).

Toxicity Studies: 7–8-week-old healthy female CD-1 mice were randomly divided into 2 groups (n = 4/group): PBS group and SSS-micelles group. 2 mg mL^{-1} 200 µL SSS-micelles solution or 200 µL PBS solution was intravenously injected into mice via tail vein, respectively. Mice health condition was monitored for 14 days. All mice were sacrificed on the 14th day after injection, then blood was collected via face piercing for CBC analysis and serum chemistry studies. Organs including heart, liver, spleen, lungs, kidneys were harvested and fixed in formalin solution for further H&E staining analysis.

PA Imaging Systems: First, an acoustic-resolution photoacoustic microscope (AR-PAM) was used for in vitro PA spectrum and in vivo 3D PA intestine imaging.[78] A laser consists of an Nd:YAG pumping source and a tunable OPO, allowing wavelengths of 532, 1064, and 680–900 nm. A focused single element US transducer with a central frequency at 5 MHz was used for PA signal acquisition. Two stepper motors performed mechanical scanning along the X and Y axes to acquire 3D PA images. Second, a clinical PA/US imaging system was used to obtain in vitro and in vivo deep tissue images.[79] A 128 elements US transducer with a central frequency at 8.5 MHz was used for 2D PA/US image acquisition. The 1064 nm wavelength of the Nd:YAG source was used as the PA excitation source, and the laser pulse energy was ≈70–80 mJ cm^{-2}.

In Vitro PA Spectrum and Deep Tissue Imaging: For in vitro PA spectrum, concentrated SSS-micelles (60 mg mL^{-1}, 100 µL 1200 O.D.) and distilled water were respectively filled in microtubes with a thickness similar to that of blood vessels, and PA responses were measured for each wavelength (700, 900 and 1064 nm). For in vitro deep tissue PA imaging, the SSS-micelles (60 mg mL^{-1}, 1 mL 1200 O.D.) was filled in a 1 mL tube. The chicken breast tissue was stacked on the tube, and 2D depth resolved PA images were acquired at specific depths (3.8, 5.2, and 6.5 cm).

In Vivo Bladder and Intestinal PA Imaging: All PA animal experiments were performed according to laboratory animal use protocols approved by the Institutional Animal Care and Use Committee (IACUC) of Pohang University of Science and Technology (POSTECH), and regulations of the National Institutes of Health Guide for the Care and Use of Laboratory Animals. Healthy rats (≈200 g) were prepared to acquire in vivo bladder PA/US images. The rats were anesthetized with isoflurane, and kept anesthetized with a vaporized-isoflurane system which consistently provides 1 L min^{-1} of oxygen and 0.75% isoflurane. After obtaining control PA images of the rat bladder, SSS-micelles were delivered to the rat bladder via transurethral injection (200 µL, 56 mg mL^{-1}). To confirm the potential of SSS-micelles as deep tissue PA imaging agents, PA images were acquired by stacking chicken breast tissue (0.5, 3, 4, and 5 cm) over the bladder of rats. The rodent fur that might generate the PA signal was gently removed before the experiment.

For intestinal imaging, mice (≈20 g) that were fasted for two days to empty their intestines were prepared to acquire 2D PA/US and 3D PA images of the intestine in vivo. 2-day fasting time was selected because it was previously reported that there is still some form of GI contents after fasting more than one-day. After these preparations including fasting, which are also needed for the commonly used clinical imaging approaches such as endoscopy, PA has shown great promise as a good and potentially realistic diagnostic method for imaging of tumors, lymph node mapping, breast, brain, and many others. The mice were anesthetized and kept anesthetized with the vaporized-isoflurane system during the experiment. After collecting control PA images, the mice were administered SSS-micelles (20 µL, 56 mg mL^{-1}) by gavage, and then PA images of the mice intestine were acquired in the same area as the control PA images. In the 2D PA/US imaging, the image depth was extended using chicken breast to confirm the deep tissue imaging capability of SSS-micelles. In 3D PA imaging, PA images were acquired over time to confirm the transit of SSS-micelles in the intestine.

Statistical Analysis: Data were analyzed by one-tailed or two tailed t-test. $p > 0.05$ is considered not statistically significant (ns),* and ** means $0.01 < p < 0.05$ and $p < 0.01$, respectively. All values were shown as mean ±standard deviation (S.D.) with indicated sample size.

© 2021 Wiley-VCH GmbH

Supporting Information

Supporting Information is available from the Wiley Online Library or from the author.

Acknowledgements

This work was supported by the National Key Research and Development Program (2021YFC 2102300), the Start-Up grant at Tianjin University, One-thousand Young Talent Program, and the National Natural Science Foundation of China (32071384) and the National Research Foundation (NRF) of Korea grants (2020R1A6A1A03047902, 2019R1A2C2006269 and BK21 FOUR Projects). The authors thank Jonathan F. Lovell for proofreading the manuscript.

Conflict of Interest

The authors declare no conflict of interest.

Author Contributions

Y.D., B.P., and J.Y. contributed equally to this work. Y.D. and Y.Z. conceived and designed the project. B.P., M.H., and C.K. designed and performed deep tissue imaging and interpreted the results. J.Y. and J.S. performed tumor photoacoustic imaging and interpreted the results. G.L. assisted organic synthesis. B.P. and Y.F. assisted characterizing the SSS-micelles. Y.D., X.W., and X.Y. conducted photothermal therapy of tumor. Y.D., X.W., and Z.J. conducted toxicity experiments. Y.D. and Y.Z. wrote the draft and all authors revised the manuscript and performed data analysis.

Data Availability Statement

The data that support the findings of this study are available on request from the corresponding author. The data are not publicly available due to privacy or ethical restrictions.

Keywords

deep tissue imaging, photoacoustic imaging, second near infrared window, semiconducting polymers, surfactant-stripped micelles

Received: July 14, 2021
Revised: October 28, 2021
Published online:

[1] T. Kuchimaru, S. Iwano, M. Kiyama, S. Mitsumata, T. Kadonosono, H. Niwa, S. Maki, S. Kizaka-Kondoh, *Nat. Commun.* **2016**, *7*, 11856.
[2] R. G. Aswathy, Y. Yoshida, T. Maekawa, D. S. Kumar, *Anal. Bioanal. Chem.* **2010**, *397*, 1417.
[3] A. Feuchtinger, A. Walch, M. Dobosz, *Histochem. Cell Biol.* **2016**, *146*, 781.
[4] B. Park, K. M. Lee, S. Park, M. Yun, H. J. Choi, J. Kim, C. Lee, H. Kim, C. Kim, *Theranostics* **2020**, *10*, 2509.
[5] L. V. Wang, S. Hu, *Science* **2012**, *335*, 1458.
[6] J. Wu, L. You, L. Lan, H. J. Lee, S. T. Chaudhry, R. Li, J. X. Cheng, J. Mei, *Adv. Mater.* **2017**, *29*, 1703403.
[7] Y. Jiang, P. K. Upputuri, C. Xie, Y. Lyu, L. Zhang, Q. Xiong, M. Pramanik, K. Pu, *Nano Lett.* **2017**, *17*, 4964.
[8] U. Chitgupi, N. Nyayapathi, J. Kim, D. Wang, B. Sun, C. Li, K. Carter, W. C. Huang, C. Kim, J. Xia, J. F. Lovell, *Adv. Mater.* **2019**, *31*, 1902279.
[9] C. Kim, C. Favazza, L. V. Wang, *Chem. Rev.* **2010**, *110*, 2756.
[10] W. Li, X. Chen, *Nanomedicine* **2015**, *10*, 299.
[11] A. De La Zerda, C. Zavaleta, S. Keren, S. Vaithilingam, S. Bodapati, Z. Liu, J. Levi, B. R. Smith, T.-J. Ma, O. Oralkan, Z. Cheng, X. Chen, H. Dai, B. T. Khuri-Yakub, S. S. Gambhir, *Nat. Nanotechnol.* **2008**, *3*, 557.
[12] L. Zhang, D. Sheng, D. Wang, Y. Yao, K. Yang, Z. Wang, L. Deng, Y. Chen, *Theranostics* **2018**, *8*, 1591.
[13] S. Diao, G. Hong, A. L. Antaris, J. L. Blackburn, K. Cheng, Z. Cheng, H. Dai, *Nano Res.* **2015**, *8*, 3027.
[14] A. Zebibula, N. Alifu, L. Xia, C. Sun, X. Yu, D. Xue, L. Liu, G. Li, J. Qian, *Adv. Funct. Mater.* **2018**, *28*, 1703451.
[15] A. Sun, H. Guo, Q. Gan, L. Yang, Q. Liu, L. Xi, *Opt. Express* **2020**, *28*, 9002.
[16] H. Wan, J. Yue, S. Zhu, T. Uno, X. Zhang, Q. Yang, K. Yu, G. Hong, J. Wang, L. Li, Z. Ma, H. Gao, Y. Zhong, J. Su, A. L. Antaris, Y. Xia, J. Luo, Y. Liang, H. Dai, *Nat. Commun.* **2018**, *9*, 1171.
[17] S. Zhu, R. Tian, A. L. Antaris, X. Chen, H. Dai, *Adv. Mater.* **2019**, *31*, 1900321.
[18] S. Zhu, B. C. Yung, S. Chandra, G. Niu, A. L. Antaris, X. Chen, *Theranostics* **2018**, *8*, 4141.
[19] F. Zhang, Y. Chen, P. Pei, Z. Lei, X. Zhang, D. Yin, *Angew. Chem., Int. Ed. Engl.* **2021**, *60*, 15809.
[20] L. Lu, B. Li, S. Ding, Y. Fan, S. Wang, C. Sun, M. Zhao, C. X. Zhao, F. Zhang, *Nat. Commun.* **2020**, *11*, 4192.
[21] Y. Yang, S. Wang, L. Lu, Q. Zhang, P. Yu, Y. Fan, F. Zhang, *Angew. Chem., Int. Ed. Engl.* **2020**, *59*, 18380.
[22] B. Guo, J. Chen, N. Chen, E. Middha, S. Xu, Y. Pan, M. Wu, K. Li, C. Liu, B. Liu, *Adv. Mater.* **2019**, *31*, 1808355.
[23] Y. Jiang, J. Li, X. Zhen, C. Xie, K. Pu, *Adv. Mater.* **2018**, *30*, 1705980.
[24] W. Zhang, X. Sun, T. Huang, X. Pan, P. Sun, J. Li, H. Zhang, X. Lu, Q. Fan, W. Huang, *Chem. Commun.* **2019**, *55*, 9487.
[25] Q. Miao, K. Pu, *Adv. Mater.* **2018**, *30*, 1801778.
[26] K. Shou, Y. Tang, H. Chen, S. Chen, L. Zhang, A. Zhang, Q. Fan, A. Yu, Z. Cheng, *Chem. Sci.* **2018**, *9*, 3105.
[27] H. Wan, H. Ma, S. Zhu, F. Wang, Y. Tian, R. Ma, Q. Yang, Z. Hu, T. Zhu, W. Wang, Z. Ma, M. Zhang, Y. Zhong, H. Sun, Y. Liang, H. Dai, *Adv. Funct. Mater.* **2018**, *28*, 1804956.
[28] P. Wang, Y. Fan, L. Lu, L. Liu, L. Fan, M. Zhao, Y. Xie, C. Xu, F. Zhang, *Nat. Commun.* **2018**, *9*, 2898.
[29] B. Guo, Z. Sheng, D. Hu, C. Liu, H. Zheng, B. Liu, *Adv. Mater.* **2018**, *30*, 1802591.
[30] B. Guo, Z. Feng, D. Hu, S. Xu, E. Middha, Y. Pan, C. Liu, H. Zheng, J. Qian, Z. Sheng, B. Liu, *Adv. Mater.* **2019**, *31*, 1902504.
[31] Z. Feng, X. Yu, M. Jiang, L. Zhu, Y. Zhang, W. Yang, W. Xi, G. Li, J. Qian, *Theranostics* **2019**, *9*, 5706.
[32] B. Du, C. Qu, K. Qian, Y. Ren, Y. Li, X. Cui, S. He, Y. Wu, T. Ko, R. Liu, X. Li, Y. Li, Z. Cheng, *Adv. Opt. Mater.* **2019**, *8*, 1901471.
[33] S. Zhu, S. Herraiz, J. Yue, M. Zhang, H. Wan, Q. Yang, Z. Ma, Y. Wang, J. He, A. L. Antaris, Y. Zhong, S. Diao, Y. Feng, Y. Zhou, K. Yu, G. Hong, Y. Liang, A. J. Hsueh, H. Dai, *Adv. Mater.* **2018**, *30*, 1705799.
[34] Y. Zhou, D. Wang, Y. Zhang, U. Chitgupi, J. Geng, Y. Wang, Y. Zhang, T. R. Cook, J. Xia, J. F. Lovell, *Theranostics* **2016**, *6*, 688.
[35] Y. Lyu, X. Zhen, Y. Miao, K. Pu, *ACS Nano* **2017**, *11*, 358.
[36] J. Zhang, X. Zhen, P. K. Upputuri, M. Pramanik, P. Chen, K. Pu, *Adv. Mater.* **2017**, *29*, 1604764.
[37] S. Wang, Z. Li, Y. Liu, G. Feng, J. Zheng, Z. Yuan, X. Zhang, *Sens. Actuators, B* **2018**, *267*, 403.
[38] D. Li, S. Wang, Z. Lei, C. Sun, A. M. El-Toni, M. S. Alhoshan, Y. Fan, F. Zhang, *Anal. Chem.* **2019**, *91*, 4771.
[39] J. Chen, J. Qi, C. Chen, J. Chen, L. Liu, R. Gao, T. Zhang, L. Song, D. Ding, P. Zhang, C. Liu, *Adv. Mater.* **2020**, *32*, 2003399.
[40] L. Zhang, S. Gao, F. Zhang, K. Yang, Q. Ma, L. Zhu, *ACS Nano* **2014**, *8*, 12250.
[41] D. Gao, Z. Sheng, Y. Liu, D. Hu, J. Zhang, X. Zhang, H. Zheng, Z. Yuan, *Adv. Healthcare Mater.* **2016**, *6*, 1601094.

 © 2021 Wiley-VCH GmbH

[42] G. Liu, J. Zhu, H. Guo, A. Sun, P. Chen, L. Xi, W. Huang, X. Song, X. Dong, *Angew. Chem., Int. Ed. Engl.* **2019**, *58*, 18641.
[43] X. Cheng, R. Sun, L. Yin, Z. Chai, H. Shi, M. Gao, *Adv. Mater.* **2017**, *29*, 1604894.
[44] J. Zhou, Y. Jiang, S. Hou, P. K. Upputuri, D. Wu, J. Li, P. Wang, X. Zhen, M. Pramanik, K. Pu, *ACS Nano* **2018**, *12*, 2643.
[45] Q. Chen, J. Chen, Z. Yang, L. Zhang, Z. Dong, Z. Liu, *Nano Res.* **2018**, *11*, 5657.
[46] Z. Cao, L. Feng, G. Zhang, J. Wang, S. Shen, D. Li, X. Yang, *Biomaterials* **2018**, *155*, 103.
[47] C. Yin, G. Wen, C. Liu, B. Yang, S. Lin, J. Huang, P. Zhao, S. H. D. Wong, K. Zhang, X. Chen, G. Li, X. Jiang, J. Huang, K. Pu, L. Wang, L. Bian, *ACS Nano* **2018**, *12*, 12201.
[48] T. Sun, J. H. Dou, S. Liu, X. Wang, X. Zheng, Y. Wang, J. Pei, Z. Xie, *ACS Appl. Mater. Interfaces* **2018**, *10*, 7919.
[49] B. Guo, Z. Sheng, K. Kenry, D. Hu, X. Lin, S. Xu, C. Liu, H. Zheng, B. Liu, *Mater. Horiz.* **2017**, *4*, 1151.
[50] X. Yu, A. Li, C. Zhao, Y. Kai, W. Li, *ACS Nano* **2017**, *11*, 3990.
[51] H. Lin, S. Gao, C. Dai, Y. Chen, J. Shi, *Niobium Compd.* **2017**, *139*, 16235.
[52] D. Yao, Y. Wang, R. Zou, K. Bian, P. Liu, S. Shen, W. Yang, B. Zhang, D. Wang, *ACS Appl. Mater. Interfaces* **2020**, *12*, 4276.
[53] L. Ma, S. Huang, S. He, Z. Wang, Z. Cheng, *Biosens. Bioelectron.* **2020**, *151*, 112000.
[54] R. Wang, L. Zhou, W. Wang, X. Li, F. Zhang, *Nat. Commun.* **2017**, *8*, 14702.
[55] N. Bhutiani, A. Samykutty, K. M. McMasters, N. K. Egilmez, L. R. McNally, *Photoacoustics* **2019**, *13*, 46.
[56] Z. Jiang, B. Sun, Y. Wang, H. Gao, H. Ren, H. Zhang, T. Lu, X. Ren, W. Wei, X. Wang, L. Zhang, J. Li, D. Ding, J. F. Lovell, Y. Zhang, *Adv. Healthcare Mater.* **2021**, 2100356.
[57] F.-Z. Cui, J.-H. Liu, Y. Liu, B.-Y. Yuan, X. Gong, Q.-H. Yuan, T.-T. Gong, L. Wang, *Chinese J. Anal. Chem.* **2020**, *48*, 1004.
[58] Y. Jiang, J. Huang, C. Xu, K. Pu, *Nat. Commun.* **2021**, *12*, 742.
[59] C. Xu, K. Pu, *Chem. Soc. Rev.* **2021**, *50*, 1111.
[60] C. Zhang, Z. Zeng, D. Cui, S. He, Y. Jiang, J. Li, J. Huang, K. Pu, *Nat. Commun.* **2021**, *12*, 2934.
[61] M. Xu, C. Zhang, Z. Zeng, K. Pu, *ACS Appl. Polym. Mater.* **2021**, *3*, 4375.
[62] X. Dang, N. M. Bardhan, J. Qi, L. Gu, N. A. Eze, C.-W. Lin, S. Kataria, P. T. Hammond, A. M. Belcher, *Sci. Rep.* **2019**, *9*, 3873.
[63] P. Howes, M. Green, J. Levitt, K. Suhling, M. Hughes, *J. Am. Chem. Soc.* **2010**, *132*, 3989.
[64] C. Wu, S. J. Hansen, Q. Hou, J. Yu, M. Zeigler, Y. Jin, D. R. Burnham, J. D. McNeill, J. M. Olson, D. T. Chiu, *Angew. Chem., Int. Ed. Engl.* **2011**, *50*, 3430.
[65] K. Pu, J. Mei, J. V. Jokerst, G. Hong, A. L. Antaris, N. Chattopadhyay, A. J. Shuhendler, T. Kurosawa, Y. Zhou, S. S. Gambhir, Z. Bao, J. Rao, *Adv. Mater.* **2015**, *27*, 5184.
[66] Y. Jiang, P. K. Upputuri, C. Xie, Z. Zeng, A. Sharma, X. Zhen, J. Li, J. Huang, M. Pramanik, K. Pu, *Adv. Mater.* **2019**, *31*, 1808166.
[67] K. Pu, A. J. Shuhendler, J. V. Jokerst, J. Mei, S. S. Gambhir, Z. Bao, J. Rao, *Nat. Nanotechnol.* **2014**, *9*, 233.
[68] X. D. Zhang, H. Wang, A. L. Antaris, L. Li, S. Diao, R. Ma, A. Nguyen, G. Hong, Z. Ma, J. Wang, S. Zhu, J. M. Castellano, T. Wyss-Coray, Y. Liang, J. Luo, H. Dai, *Adv. Mater.* **2016**, *28*, 6872.
[69] Y. Zhang, M. Jeon, L. J. Rich, H. Hong, J. Geng, Y. Zhang, S. Shi, T. E. Barnhart, P. Alexandridis, J. D. Huizinga, M. Seshadri, W. Cai, C. Kim, J. F. Lovell, *Nat. Nanotechnol.* **2014**, *9*, 631.
[70] Y. Zhang, D. Wang, S. Goel, B. Sun, U. Chitgupi, J. Geng, H. Sun, T. E. Barnhart, W. Cai, J. Xia, J. F. Lovell, *Adv. Mater.* **2016**, *28*, 8524.
[71] H. Maeda, J. Wu, T. Sawa, Y. Matsumura, K. Hori, *J. Controlled Release* **2000**, *65*, 271.
[72] M. C. O. da Rocha, P. B. da Silva, M. A. Radicchi, B. Y. G. Andrade, J. V. de Oliveira, T. Venus, C. Merker, I. Estrela-Lopis, J. P. F. Longo, S. N. Báo, *J. Nanobiotechnol.* **2020**, *18*, 43.
[73] S. Park, G. Park, J. Kim, W. Choi, U. Jeong, C. Kim, *Nanoscale* **2018**, *10*, 20548.
[74] S. Cho, J. Baik, R. Managuli, C. Kim, *Photoacoustics* **2020**, *18*, 100168.
[75] M. Jeon, S. Jenkins, J. Oh, J. Kim, T. Peterson, J. Chen, C. Kim, *Nanomedicine* **2013**, *9*, 1377.
[76] Y. Zhang, W. Song, J. Geng, U. Chitgupi, H. Unsal, J. Federizon, J. Rzayev, D. K. Sukumaran, P. Alexandridis, J. F. Lovell, *Nat. Commun.* **2016**, *7*, 11649.
[77] W. Zhang, T. Huang, J. Li, P. Sun, Y. Wang, W. Shi, W. Han, W. Wang, Q. Fan, W. Huang, *ACS Appl. Mater. Interfaces* **2019**, *11*, 16311.
[78] D. Lee, S. Beack, J. Yoo, S.-K. Kim, C. Lee, W. Kwon, S. K. Hahn, C. Kim, *Adv. Funct. Mater.* **2018**, *28*, 1800941.
[79] C. Lee, W. Choi, J. Kim, C. Kim, *Photoacoustics* **2020**, *18*, 100173.

© 2021 Wiley-VCH GmbH